https://doi.org/10.1016/j.chempr.2018.01.002

Coupled *s-p-d* Exchange in Facet-Controlled Pd_3Pb Tripods Enhances Oxygen Reduction Catalysis

Lingzheng Bu,[1] Qi Shao,[1] Yecan Pi,[1] Jianlin Yao,[1] Mingchuan Luo,[2,3] Jianping Lang,[1] Sooyeon Hwang,[4] Huolin Xin,[4] Bolong Huang,[5*] Jun Guo,[6] Dong Su,[4*] Shaojun Guo,[2,3*] and Xiaoqing Huang[1*]

[1]College of Chemistry, Chemical Engineering and Materials Science, Soochow University, Jiangsu 215123, China.

[2]Department of Materials Science & Engineering, College of Engineering, Peking University, Beijing 100871, China.

[3]BIC-ESAT, College of Engineering, Peking University, Beijing 100871, China.

[4]Center for Functional Nanomaterials, Brookhaven National Laboratory, Upton, New York 11973, United States.

[5]Department of Applied Biology and Chemical Technology, Hong Kong Polytechnic University, Hung Hom, Kowloon, Hong Kong SAR, China.

[6]Testing & Analysis Center, Soochow University, Jiangsu 215123, China.

*Correspondence and requests for materials should be addressed to B.L.H., D.S., S.J.G., and X.Q.H. (bhuang@polyu.edu.hk; dsu@bnl.gov; guosj@pku.edu.cn; hxq006@suda.edu.cn).

SUMMARY

Highly efficient oxygen reduction reaction (ORR) catalysts are the key in developing high-performance fuel cells and metal-air batteries. Palladium (Pd) is a class of catalyst system for ORR with its potential to replace more expensive and rare platinum (Pt), however it usually exhibits much lower ORR electrocatalytic activity than Pt. Herein, we report a class of structurally ordered Pd_3Pb tripods (TPs) with dominated {110} facets that show extremely high activity and stability for ORR in alkaline condition. Totally different from the well-known knowledge that excellent ORR activity of Pt catalyst is caused by its partially-filled *d*-orbital, our first principle calculations suggest that the strong charge exchange between Pd-4*d* and Pb-(*sp*) orbitals on {110} facet of Pd_3Pb TPs results in the Pd-Pb local bonding unit with the orbital configuration similar to Pt. As a consequence, the Pd_3Pb TPs exhibit much higher specific and mass activities for ORR than those of commercial Pt/C and commercial Pd/C. The Pd_3Pb TPs are rather endurable for ORR and sustain over 20,000 potential cycles under alkaline condition with negligible structural and compositional changes.

KEYWORDS: palladium, lead, tripod, facet control, *s-p-d* exchange, oxygen reduction reaction

INTRODUCTION

Highly efficient catalysts for oxygen reduction reaction (ORR) are the most decisive factor in high-performance fuel cells in order to meet contemporary energy supplies and industrial needs.[1-8]

Platinum (Pt) is the most efficient ORR catalyst for fuel cells due to its partially-filled *d*-orbital (Pt-5$d^{8\sim9}$) accounted for prominent electro- (electron transfer) and thermo-reactivity (chemisorption).[9-14] However, the high cost and limited reservation of Pt on earth become the uncompromised obstruction for practical fuel cell devices, and great efforts have been devoted to exploring low-cost alternatives.[4, 15-19] Since the electronic transfer determines the kinetic rate in the ORR, the non-Pt based catalysts such as transition metal carbides (TMC) [Ref1] and nitrides (TMN) [Ref2-4] are highly competitive, because of the promising anti-corrosion and the feasibility of tuning the *d*-electron activity with *s*-*d* hybridization giving like Pt-like behavior with active charge transferability. This creates an opportunity of further importing coupled *s*-*p*-*d* hybridization ensuring the more directionless preference within a longer ranged order charge exchange for the catalysis, even the completely occupied and natively inert d^{10} orbitals. Palladium (Pd) has recently been proposed to catalyze ORR well in alkaline solutions. Despite the intensive efforts in the synthesis, the ORR catalytic activities of Pd catalysts are still far lower than those of Pt ones.[20-22] This is intrinsically due to the different surface electronic structures between Pd and Pt: The t_{2g} component in 4d^{10} configuration of Pd lies too deep to effectively overlap with O-2*p* orbitals of oxygen absorbance, resulting in the slow electron transfer rate and weakened oxygen binding energy during ORR process.[23] This is the key mechanism why Pd usually exhibits much lower electrocatalytic activity for ORR than Pt, and remains an exception and uninerpretable by *d*-band theory. In this regard, precisely tuning the 4d^{10} configuration of Pd similar to that of Pt for facilitating the electron transfer rate to achieve much better ORR activity is highly desirable, *yet* a formidable challenge.

Herein, we report a class of $L1_2$-ordered Pd_3Pb tripods (TPs) with dominated {110} facets that can achieve the unprecedented electrocatalytic activity for ORR in alkaline solution. Totally different from the well-known knowledge that excellent ORR activity of Pt catalyst is caused by its partially-filled *d*-orbital, which gives good charge transfer (electro-activity) with least over-binding energy for intermediate adsorbates (thermo-activity) in metals, our first principle calculations indicate that the ORR activity enhancement in the Pd_3Pb TPs can be attributed to a new strong coupled *s-p-d* exchange effect on their {110} facets. This inter-orbital coupling effect can propel the electrons from inert closed-shell $4d^{10}$ orbital, and activate the Pd site to break-through the constrained electronic transfer from short-range order into long-range one without the barrier on the reacting surface, which makes the Pd_3Pb TPs exhibit 6.7 and 13.4 times higher mass and specific activities for ORR than those of Pt/C, and 8.4 and 12.0 times higher mass and specific activities for ORR than those of Pd/C, respectively. They are highly durable for ORR with negligible activity decay and limited structure and composition changes over 20,000 potential cycles. To the best of our knowledge, the present Pd_3Pb TPs are the most active and stable non-Pt catalysts for ORR reported to date.

RESULTS AND DISCUSSION

Morphological and Structural Analyses of Ordered Pd_3Pb TPs

A wet-chemical approach was used to make the Pd_3Pb TPs by the use of $Pd(acac)_2$ and $Pb(acac)_2$ as precursors, phloroglucinol as reducing agent, oleylamine (OAm) and oleic acid (OA) as mixed solvents

and surfactants (see the Experimental Procedures section for details). We found that the proper precursors, reducing agents and solvents are the key factors in preparing well-defined ordered Pd_3Pb TPs (**Figures S1-S7**). Transmission electron microscopy (TEM) images (**Figure 1A and Figure S8A,B**) show the tripod-like morphology is dominated with a chemical yield approaching 90%. **Figure S8C,D** are the representative high-angle annular dark-field scanning TEM (HAADF-STEM) images of the Pd-Pb TPs. The branches of the Pd-Pb TPs have an average diameter of 7.8 nm and an average length of 56.8 nm (**Figure S8E,F**). The power X-ray diffraction (PXRD) of Pd-Pb TPs (**Figure 1B**) shows the distinct diffraction peaks, assigned to the (100), (110), (210), (211), (221) and (310) reflections. The intensity ratio of the (110) to (111) peaks, indicating the degree of ordering,[24] is measured as 0.062 for the Pd-Pb TPs, close to the ratio of 0.063 determined from X-ray pattern of bulk reference (JCPDS No. 03-065-3259), indicating that the Pd-Pb TPs are fully $L1_2$-ordered with Pm-3m (221) space group. Inductively Coupled Plasma-Atomic Emission Spectrometry (ICP-AES) measurements reveal that the molar ratio of Pd to Pb in the Pd-Pb TPs is 74.5/25.5. The TEM energy-dispersive X-ray spectroscopy (TEM-EDS) (**Figure S8G**) and scanning TEM-electron energy-loss spectroscopy (STEM-EELS) mappings confirm that Pd and Pb distribute homogeneously throughout the whole TP (**Figure 1C and Figure S9**). We performed the three-dimensional (3D) STEM electron tomography (**Figure 1D and video S1**) to identify the crystallographic feature of TPs: It is shown that two branches of the tripod have <111> type growth directions, $[\bar{1}1\bar{1}]$ and $[1\bar{1}\bar{1}]$, while the third one is [001] orientated. The angle between the [001] branch and <111> ones is measured as 125°, and the angle between two <111>

branches is measured as 110°, in consistent with the atomic model (**Figure 1E**) and 3D illustration (**Figure 1F**) based on Pm-3m phase. By comparing the cross-sectional planes (**Figure 1G,H**) and the corresponding atomic models (**Figure 1I,J**) of these branches, we found that the {110} facets are enriched on two <111> branches and one [100] branch is dominated with {100} facets.

High-resolution HAADF-STEM and TEM imaging techniques were utilized to further reveal the atomic structures on the surfaces of the branches (**Figure 2 and Figures S10-S12**). According to the 3D tomography model (**Figure 1D**), the atomic stacking on these branches can only be viewed along the <100> and <112> axes. Therefore, besides the <110> zone axis normal to the TP, we took the low-magnification (S)TEM images along the edge-on condition for the [001] and $[\bar{1}1\bar{1}]$ branches, namely <100> and <112> zone axes (**Figure 2A**,**E**,**I**), respectively. The projections of the atomic model along these three zone axes (**Figure 2B**,**F**,**J**) are in consistent with the morphologies revealed in (S)TEM images along the corresponding directions. High-resolution HAADF-STEM images from the <100>, <110> and <112> zone axes (**Figure 2C-D**,**G-H**,**K-L**) clearly reveal the $L1_2$ ordering of Pd and Pb atoms inside TPs as well as the dominated {110} facet on two <111> branches and {100} facets on the <100> branch. These HR-STEM images (**Figure 2**) and STEM-EELS line scan (**Figure S13**) show no secondary phase or atomic reconstructions, indicating the Pd-terminated surfaces of Pd_3Pb TPs are thermodynamically stable. Those advanced electron microscopy characterizations collectively reveal the successful creation of a unique class of highly ordered Pd-Pb TPs with dominated {110} facets.

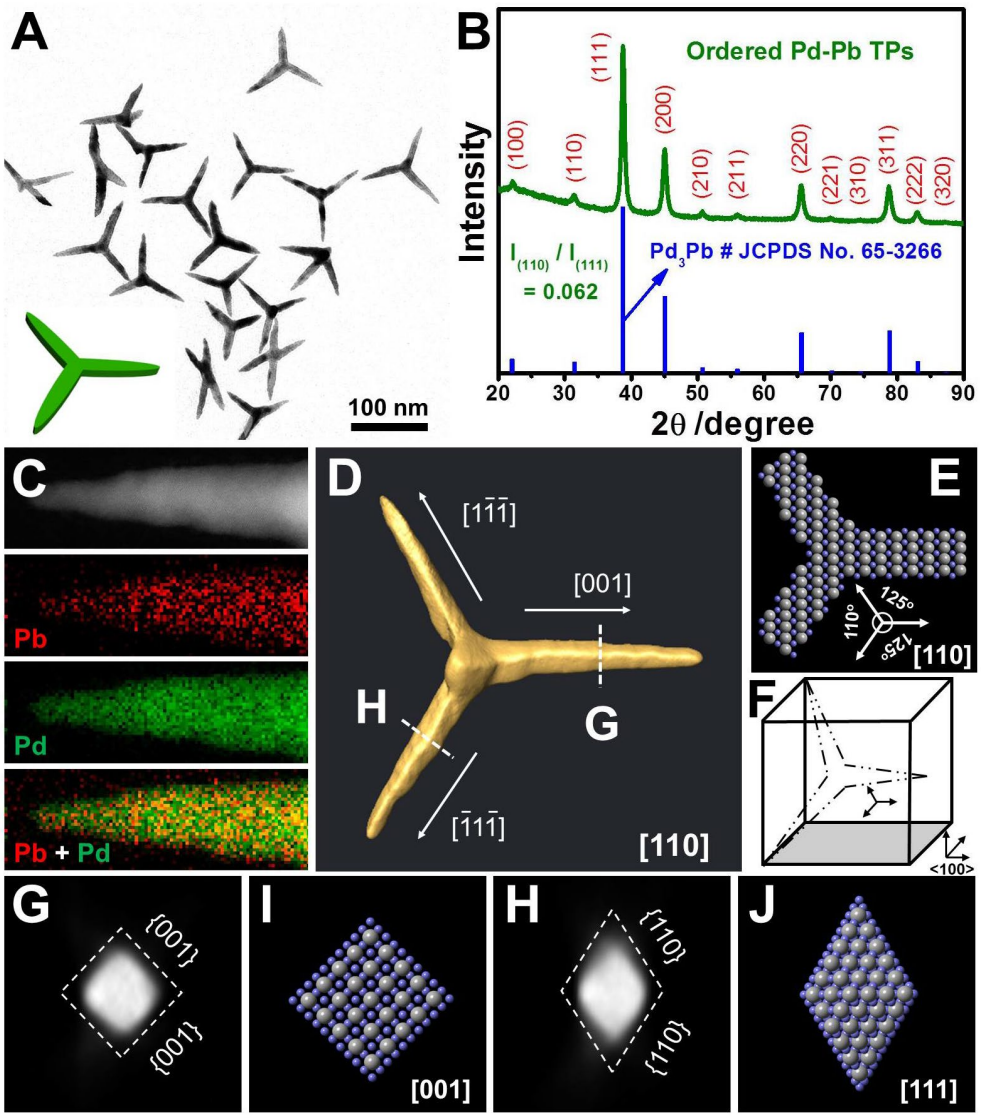

Figure 1. Morphological and Structural Characterizations of Pd-Pb TPs. (**A**) TEM image, (**B**) PXRD pattern, (**C**) STEM-EELS elemental mappings, (**D**) reconstructed 3D tomograms along <110> zone axis, (**E**) atomic model along <110> zone axis, (**F**) 3D illustration along <100> zone axis, and cross-sectinoal reconstructed planes and corresponding atomic models of (**G**, **I**) the <100> fork and (**H**, **J**) <111> fork of the Pd_3Pb TPs.

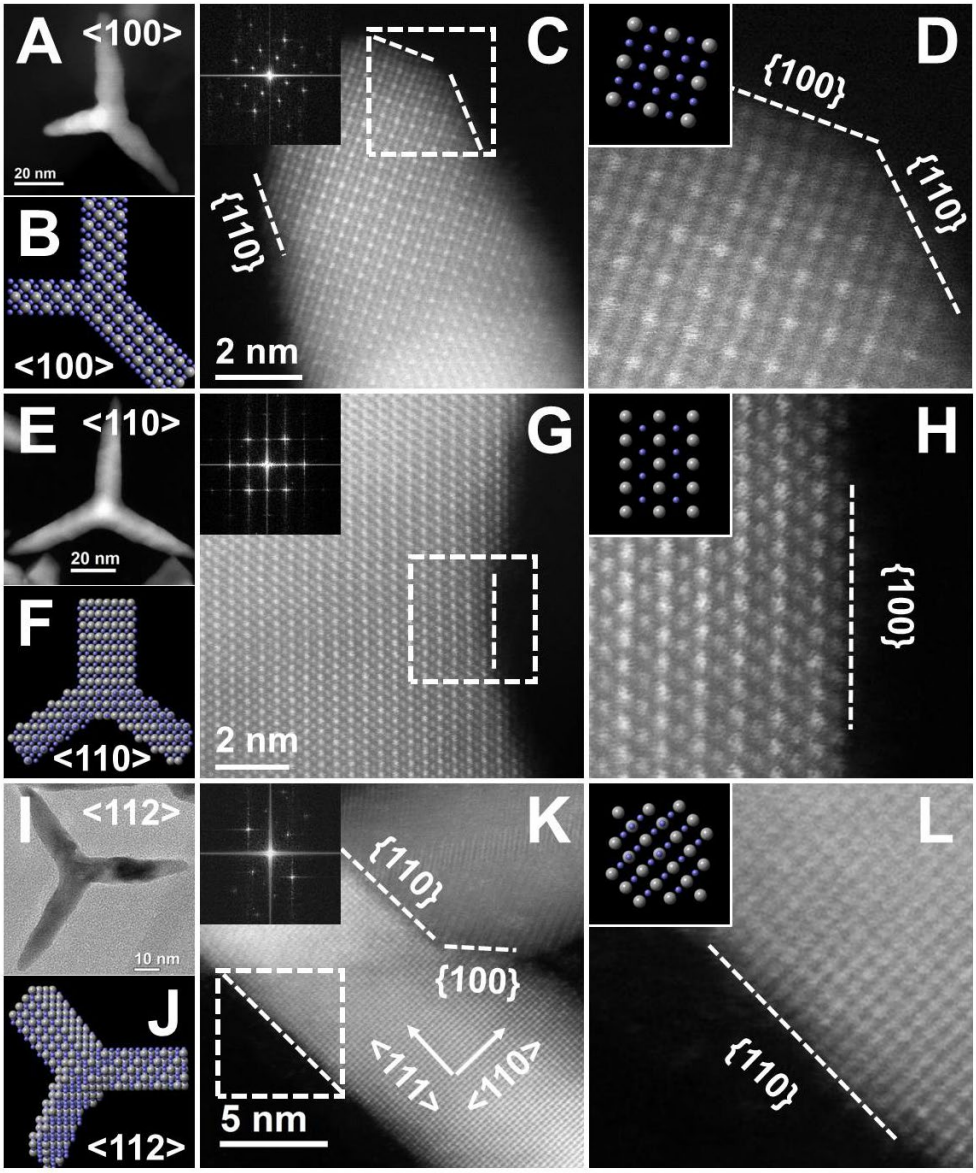

Figure 2. Atomic Structure of Pd-Pb TPs. (**A**, **E**, **I**) Low-magnification HAADF-STEM/TEM images, (**B**, **F**, **J**) the corresponding atomic models and (**C**, **G**, **K**) high-resolution HAADF-STEM images of the Pd_3Pb TP along <100>, <110> and <112> zone axes. (**D**, **H**, **L**) The enlarged HAADF-STEM images of selected areas in (**C**, **G**, **K**) respectively. Dominated facets of {100} and {110} planes are marked.

ORR Performance of Pd_3Pb TPs/C and Pd_3Pb NPs/C

In order to evaluate the ORR performance, the Pd_3Pb TPs and Pd_3Pb nanoparticles (NPs) (averaged size ~10.2 nm) (**Figure S14**) were loaded onto the commercial carbon black (C, Vulcan XC-72R), and then washed with the ethanol/acetic acid mixture (see the Methods section for details). Such treatments allowed Pd_3Pb nanocrystals (NCs) uniformly distributed on C with unchanged shapes and compositions (**Figures S15-S17**). The CO stripping experiments reveal the Pd_3Pb TPs/C has electrochemically active surface areas (ECSAs) of 31.9 $m^2\ g^{-1}$, better than those of Pd_3Pb NPs/C (28.9 $m^2\ g^{-1}$) due to their highly-open structure with thin building block, but lower than those of commercial Pt/C (63.7 $m^2\ g^{-1}$) and commercial Pd/C (45.7 $m^2\ g^{-1}$) (**Figure 3A**). **Figure 3B** shows the ORR polarization curves of Pd_3Pb TPs/C, Pd_3Pb NPs/C and Pt/C, performed at room temperature in an O_2-saturated 0.1 M KOH solution. At 0.90 V *vs.* reversible hydrogen electrode (RHE), the Pd_3Pb TPs/C exhibits the largest mass activity of 0.56 A mg_{Pd}^{-1}, 3.1, 6.7, and 8.4 times higher than those of the Pd_3Pb NPs/C (0.181 A mg_{Pd}^{-1}), commercial Pt/C (0.083 A mg_{Pt}^{-1}), and commercial Pd/C (0.067 A mg_{Pt}^{-1}), respectively (**Figure 3C and Table S1**). The ORR specific activity of the Pd_3Pb TPs/C reaches 1.76 mA cm^{-2}, 2.8, 13.4, and 12.0 times higher than those of the Pd_3Pb NPs/C, commercial Pt/C, and commercial Pd/C, respectively. The Pd_3Pb TPs/C shows the highest ORR activity among all the Pd-based catalysts reported to date in alkaline condition (**Table S2**), even better than many Pt-based electrocatalysts (**Table S3**).

We further measured the ORR stability of Pd_3Pb TPs/C, Pd_3Pb NPs/C as well as commercial Pt/C (**Figure 3D and Figure S18**). After 20,000 cycles of accelerating durability test (ADT), the Pd_3Pb TPs/C catalyst has only 16.6% loss of mass activity, while the Pd_3Pb NPs/C, Pt/C, and Pd/C show as large as 40.9%, 55.4%, and 62.7% losses in their mass activities (**Figure 3E**). These four catalysts after 20,000 ADTs were also investigated by TEM, SEM-EDX and STEM-EDX elemental mappings. There were no obvious changes on both the composition and structure of Pd_3Pb TPs (**Figures S19-S20**) after 20,000 cycles. However, under the same condition, the Pd_3Pb NPs and the commercial Pt NPs as well as the commercial Pd NPs showed obvious aggregation and grow up after durability tests (**Figures S21-S23**), further demonstrating the outstanding stability of the Pd_3Pb TPs.

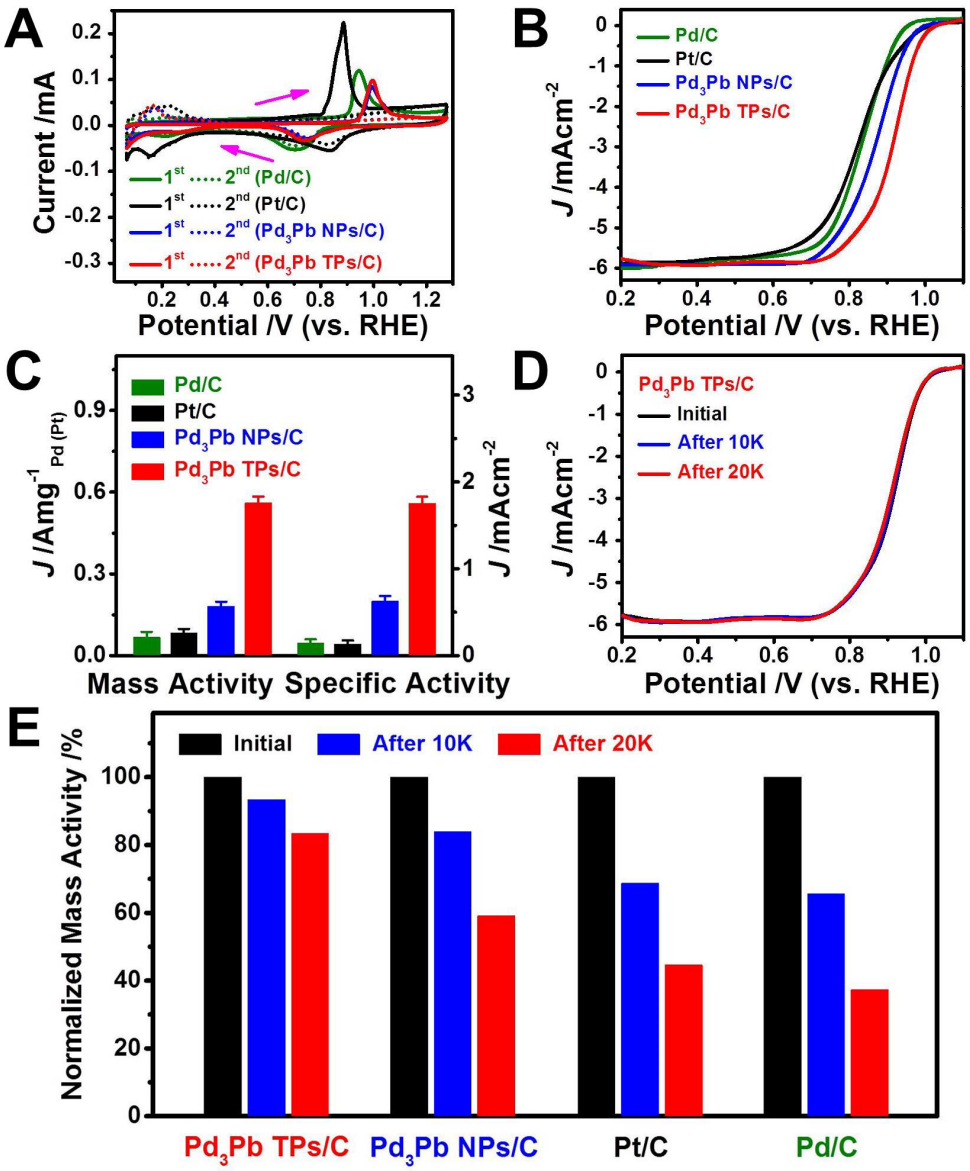

Figure 3. ORR Performance of Ordered Pd-Pb TPs/C, Pd-Pb NPs/C, Pt/C and Pd/C. (**A**) CO stripping curves, (**B**) ORR polarization curves and (**C**) histogram of mass and specific activities of different electrocatalysts. The activities and standard deviations were calculated based on five parallel measurements after Ohmic drop correction. (**D**) ORR polarization curves of Pd_3Pb TPs/C before and

after various potential cycles. (**E**) The normalized mass activity changes of Pd_3Pb TPs/C, Pd_3Pb NPs/C, Pt/C and Pd/C before and after various potential cycles. The current densities in (**B**) and (**D**) were normalized to the geometric area of the Rotating Disk Electrode (RDE, 0.196 cm^2).

DFT Calculation of *s-p-d* Exchange Effect

From the theoretical point of view, an optimal ORR catalyst requires a rapid charge transfer with nearly thermoneutral chemisorption energy ($\Delta G \sim 0$) on the reacting surface, which means that small activation barrier and removing intermediate adsorbates efficiently should be guaranteed. Our density functional theory (DFT) calculations show that the Pd and Pb sites on the Pd_3Pb (110) surface are indeed undertaking a synergetic role by following the aforementioned ultimate guiding route (**Figure S24 and Figure S25**). The DFT calculation on Gibbs free energy (**Figure 4A**) shows the ORR is a four-electron process, and the overall activation energy for the electron transfer to oxygen (**Figure S25**) relies on the free energy gained at the first step. Besides, the transition state with lower barrier denoting either the hydroxyl group (OH^-) attachment or O-bond breaking relies on the moderate bonding environment to oxygen (O^{2-}) and OH^-.

According to the *d*-band center theory, the occupied *d*-orbital behavior projected on the reactive surface closely correlates the surface chemisorption and the local electron transfer, which is significant and once ever used for determining the overall ORR reactivity (**Figure S26**).[25-28] The self-consistent orbital energy calculation on Pd-4*d* demonstrates a decrease from 7.54 eV in the bulk Pd_3Pb to 10.12 eV on its

(110) surface, implying even stronger Coulomb interactions by higher electronic negativity on the Pd-4*d* orbital due to the orbital overlapping *via s-p-d* exchange that spatially beyond the original defined constrained orbitals of each individual Pd-4*d* and Pb-(*sp*) orbitals (**Figure 4B**,**C**), despite the closed-shell effect of Pd-4d^{10} is maintained.[29, 30] Alternatively, the Goodenough-Kanamori-Anderson (GKA) theory states the orbital super-exchange effect between *d*- and non-*d*- orbitals, which is more successful beyond the realm of reactive objects with partially filled *d*-bands. Here, we proposed a coupled *s-p-d* exchange effect accounting for accelerating the electron transfer between the surface and the absorbing molecules *via* inter-orbital overlapping. This coupled *s-p-d* exchange effect was used to interpret the anti-ferromagnetism effect of 3*d*- or even 4*f*-orbital based metal oxides.[31-33] The abnormal electronegativity fluctuation through such coupled *s-p-d* exchange effect is demonstrated in terms of difference in orbital potentials by the self-consistent orbital energy calculation (**Figure S27**).[29, 30] We calculated the self-consistent orbital energy at different surface, and found a sequence: [Pd] < [Pd_3Pb-211] < [bulk Pd_3Pb] < [Pd_3Pb-100] < [Pd_3Pb-110]. The self-consistent orbital energy increases from 7.54 eV in the bulk Pd_3Pb (**Figure S27A**) to 10.12 eV on its (110) surface (**Figure S27B**), but decreases to 6.32 eV on the topmost layer of the Pd_3Pb (100) surface (**Figure S27C**), though the closed-shell effect of fully-occupied Pd-4d^{10} remains. This trend denotes a fast electron transfer process through inter-orbital exchange allowed by the parity rule, and benchmarks the ORR performance on different facets of Pd_3Pb TPs with the order of (110) > (100). With the support from GKA theory, the above analysis confirms that the (110) facet of Pd_3Pb-TP has the optimized *d*- band configuration

towards ORR where the conventionally inert Pd-4d^{10} orbital turns to be electroactive in charge transfer during the ORR process. It can potentially follow an equivalent atom (E.A.) model that makes Pd-Pb alloy perform a similar ORR activity of Pt-C system (**Figure 4D**).

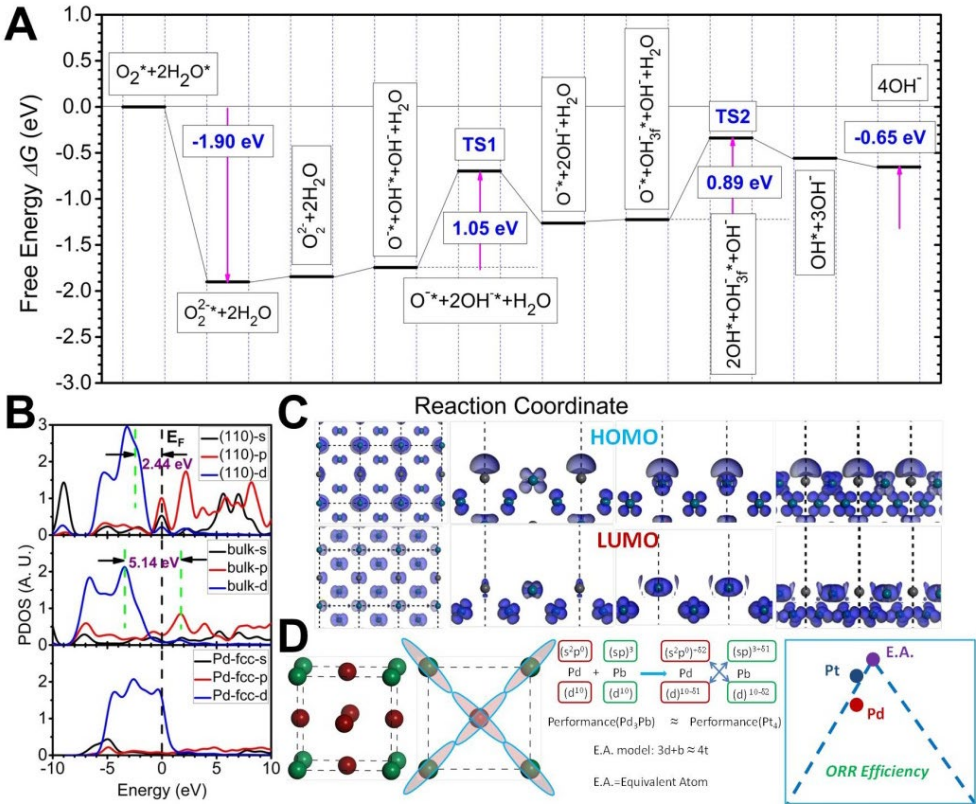

Figure 4. DFT Calculation of *s-p-d* Exchange Effect. (**A**) The Gibbs energy profiles ΔG of ORR on the Pd_3Pb (110), and the TS represents transition states. The symbol "*" denotes the molecule absorbed on the specific site of the surface. (**B**) Combined projected DOS of Pd-metal, Pd_3Pb bulk, and Pd_3Pb (110) surface. (**C**) HOMO and LUMO orbital configuration of the Pd_3Pb (110) surface with different angles of top and side views respectively (Pd = dark green, Pb = grey). (**D**) The schematic diagram and equivalent atom (E.A.) model approached by *s-p-d* exchange effect.

CONCLUSIONS

Highlighted in this report, we demonstrate the Pd_3Pb TPs with the dominated {110} facets as Pt alternative for achieving unprecedented activities and superior durability for ORR in alkaline media. They deliver the unprecedented mass activity of 0.56 A mg_{Pd}^{-1} and specific activity of 1.76 mA cm^{-2} at 0.90 V *vs.* RHE in alkaline electrolyte. The first principle calculations reveal that the coupled *s-p-d* exchange effect on {110} faceted Pd_3Pb TPs plays a decisive role in boosting ORR. The Pd_3Pb TPs exhibit high stability for ORR with negligible activity decay and structure change even after long-term 20,000 CV cycles, making them among the most active and stable non-Pt based ORR electrocatalysts reported to date. The present study opens a new route in the rational design of high-performance Pd-based nanocatalysts with proper facet/ordering control to enhance the coupled *s-p-d* exchange effect, and therefore to improve ORR catalysis.

EXPERIMENTAL PROCEDURES

Materials

Palladium(II) acetylacetonate ($Pd(acac)_2$, 99%), lead(II) acetylacetonate ($Pb(acac)_2$, 99%), oleylamine ($C_{18}H_{37}N$, OAm, > 70%), oleic acid ($C_{18}H_{34}O_2$, OA, > 85%), ascorbic acid (AA, $C_6H_8O_6$, reagent grade, 99%), 1-octadecene ($C_{18}H_{36}$, ODE, technical grade, 90%), Nafion (5%), and commercial Pd/C (10 wt% Pd) were all purchased from Sigma-Aldrich. Lead(II) chloride ($PbCl_2$, 99.99%), lead(II) acetate

trihydrate ($Pb(Ac)_2 \cdot 3H_2O$, > 99%) and phloroglucinol ($C_6H_6O_3$, ≥ 99%) were obtained from Aladdin. Commercial Pt/C (20 wt%, 2-5 nm Pt nanoparticles) was purchased from Johnson Matthey Corporation. Glucose ($C_6H_{12}O_6 \cdot H_2O$, analytical reagent), potassium hydroxide (KOH, analytical reagent, ≥ 85%), diphenyl ether ($C_{12}H_{10}O$, DPE, analytical reagent, ≥ 99.0%), cyclohexane (C_6H_{12}, analytical reagent, ≥ 99.5%), ethanol (C_2H_6O, analytical reagent, ≥ 99.7%), isopropanol (C_3H_8O, analytical reagent, ≥ 99.7%) and perchloric acid ($HClO_4$, analytical reagent, 70%-72%) were obtained from Sinopharm Chemical Reagent Co., Ltd. (Shanghai, China). All the chemicals were used as received without further purification. The water (18 MΩ/cm) used in all experiments was prepared by passing through an ultra-pure purification system. All chemicals were from commercial suppliers without further purification unless otherwise mentioned.

Preparation of Pd_3Pb tripods (Pd_3Pb TPs) and Pd_3Pb nanoparticles (Pd_3Pb NPs)

In a typical synthesis of Pd_3Pb TPs, 7.6 mg of $Pd(acac)_2$, 4.0 mg of $Pb(acac)_2$, 40.0 mg of phloroglucinol, 4.0 mL of OAm and 1.0 mL of OA were added into a vial (volume: 35 mL). After the vial had been capped, the mixture was ultrasonicated for around 120 min. The resulting homogeneous mixture was then heated from room temperature to 100 ºC in 20 min and maintained at 100 ºC for 5 h in an oil bath before it was cooled to room temperature. The Pd_3Pb TPs were collected by centrifugation and washed three times with an ethanol/cyclohexane (V/V = 9/1) mixture. For the synthesis of Pd_3Pb NPs, all the

conditions are similar to those of Pd_3Pb TPs but replacing 40.0 mg phloroglucinol with 35.6 mg AA, and using 5.0 mL OAm as the solvent/surfactant. The reaction temperature is maintained at 160 ºC.

Electrochemical measurements

The Pd_3Pb TPs or Pd_3Pb NPs dispersed in cyclohexane and Vulcan XC-72 carbon dispersed in ethanol were first mixed, and then sonicated for 1 h. The resulting Pd-Pb NCs/C was washed with the ethanol/acetic acid mixture for three times and then washed with ethanol for two times. The resulting product was dried under ambient condition, and then annealed at 250 ºC for 1 h at atmosphere condition. The final catalysts were redispersed in a mixture solvent containing isopropanol and Nafion (5%) (V / V = 1 / 0.005) to form a catalyst ink. The commercial Pt/C from JM (Pt/C, 20 wt% Pt on Vulcan XC72R carbon) and the commercial Pd/C (Pd/C, 10 wt% Pd) from Sigma-Aldrich were used as the benchmark catalysts. The concentration of Pd (Pt) was controlled to be 0.3 mg mL^{-1} based on ICP-AES measurement.

The electrochemical measurements for ORR were performed using a glassy-carbon Rotating Disk Electrode (RDE, Pine Research Instrumentation, diameter: 5 mm, area: 0.196 cm^2) connected to an installation of rotating electrode speed control (Pine Research Instrumentation, model: AFMSRCE). A leak-free saturated calomel electrode (SCE) was used as the reference electrode, and a Pt wire was used as the counter electrode. The electrolyte was 0.1 M KOH solution. The loading amounts of Pd (Pt) for the Pd_3Pb TPs/C, Pd_3Pb NPs/C, Pt/C, and Pd/C were all kept at 15.3 μg cm^{-2}. The electrochemical active

surface areas (ECSAs) of these catalysts were determined by CO stripping curves recorded at room temperature in 0.1 M $HClO_4$ solution. For the CO stripping measurements, CO gas (99.99%) was bubbled at an open circuit for 30 min in 0.1 M $HClO_4$ solution. The electrode was quickly moved to a fresh solution, and the two cycles were recorded: the first one was the CO stripping voltammetry and the second one verified the absence of residual CO in solution at a scan rate of 20 mV s^{-1} at room temperature. The CO stripping peak can be used to determine the surface area. The electrochemical surface area of the Pd (Pt) in the working electrode is calculated using Equation (1) and (2).

$$Q_{\text{co-adsorption}}(\text{C}) = \frac{\int \text{idE (mA V)}}{\text{v (mV/s)}} \qquad (1) \qquad \text{ECSA}(\text{m}^2/\text{g}) = \left[\frac{Q_{\text{co-adsorption}}(\text{C})}{210\left(\mu\frac{\text{C}}{\text{cm}^2}\right)M_{\text{Pd/Pt}}(\text{mg})}\right]10^5 \qquad (2)$$

ORR measurement was conducted in 0.1 M KOH solution purged with saturated O_2 during the measurement. The scan rate and rotation rate for ORR measurement were 10 mV s^{-1} and 1600 rpm, respectively. In the ORR polarization curves, the current densities were normalized in reference to the geometric area of the glassy carbon RDE (0.196 cm^2). For each catalyst, the kinetic current was normalized to the loading amount of Pd (Pt) and ECSA in order to generate mass and specific activities, respectively. The accelerated durability tests (ADTs) were performed at room temperature in N_2-saturated 0.1 M KOH solutions by applying the cyclic potential sweeps between 0.6 V and 1.1 V *versus* reversible hydrogen electrode (RHE) at a sweep rate of 100 mV s^{-1} for various cycles.

Calculations on Pd-4*d* orbital feature and electronic structures

(1) Electronic structure of bulk lattice of Pd_3Pb

Herein, the Pd_3Pb structure model is built based on a face-centered cubic (*fcc*) lattice. Both the internal geometry optimizations and cell relaxations were performed with default ultrafine quality. The prerequisite for the following surface catalytic process simulations is to obtain a reliable unit-cell parameter of bulk Pd_3Pb. We find the lattice space of the Pd_3Pb is 2.33 Å by first-principles calculation under BFGS algorithm, which matches well with the d-spacing of Pd_3Pb (111) planes (0.232 nm) measured in as-synthesized TPs.

With the above preliminary structure determination, the corresponding electronic structure is further estimated with anisimov-type rotational invariant DFT+U method with CASTEP code, as shown in **Figure S24**. The Hubbard U parameter has been self-consistently determined based on our previous developed method.[29, 30] The band structure (**Figure S24, left panel**) shows the nearly anisotropic metallic behavior of Pd_3Pb lattice, and is ranged from the path along high-symmetrical points (X-R-M-Γ-R). From the projected density of states (PDOS) of the bulk phase of Pd_3Pb (**Figure S24, right panel**), the Pd-4*d* orbital levels are major electronic states occupying the range from 0 to 8 eV below the E_F (0 eV). In contrast, the Pb-5*d* orbital level is stayed at 17 eV below the E_F, which is a rather deep level with negligible effect on E_F. Besides, some obvious couplings between *s-p* and *d* orbitals from 0 to 8 eV are observed below the E_F.

(2) ORR catalytic mechanism on Pd_3Pb (110) facet

The charge transfer and energy evolution mechanism of ORR on the Pd_3Pb (110) will be discussed as follows (**Figure S25**). The (110) surface is the predominant portion for the TP verified experimentally. With the energy varying with charge transfer (**Figure S25)**, the ORR on the Pd_3Pb (110) surface is actually a four electron (4e) process.

Particularly illustrated in **Figure S25**, the first step of the spontaneous two-electron transfer has the largest energy drop for the free energy of overall system, 1.90 eV below the initial level (0 eV). For the whole simulated ORR steps, it is found that there are at least two transition states (TSs) in this 4e-transfer process. The individual energy barriers of the two TS are 1.05 eV and 0.89 eV respectively, or 0.97 eV in average.

To have more detailed view, the structural configurations of two TS are (O^{-}*+$2OH^{-}$*+H_2O) and (2OH*+OH^{-}_{3f}*+H_2O), respectively. The "3f" denotes the 3-fold coordinated bonding with Pb site. The final step of the $4OH^{-}$ is obtained with ΔG stayed at the 0.65 eV below the initial energy level (0 eV) for the whole system. Meanwhile, such energy level of the final step is determined by the structural configuration that all of the hydroxyl groups (OH^{-}) are freely detached from the Pd_3Pb (110) surface.

(3) Coupled "*s*-*p*-*d*" exchange effect on Pd_3Pb (110) surface

As for the prospects of first-step charge transfer and overall small ΔG, the theoretical images were tactfully elucidated with our orbital energy calculation algorithm, insightfully interpreting that the

position of the d-band center is closely related to the strength of the absorption. It directly confirms that the larger the value of the *d*-band center (the deeper below the E_F), the weaker of the absorption presents for the external molecules like O_2. Note, the stronger absorption capability will hinder the further desorption of current absorbates or absorptions of new molecules during the four electron ORR process. But our physical images show that it is obviously different for the Pd_3Pb (110) surface. There are two different sites on the surface such as Pd and Pb, respectively. The charge transfer is existed in different forms between Pd-O and Pb-O, which does not follow the case in pure metal surfaces (*e.g.* Pt, Pd) exactly.

As shown in **Figure S26**, it is found that the *s-p* orbital has already been hybridized between Pd and Pb sites on the topmost layer of (110) surface. The *d*-band center of the system is mainly contributed from the Pd sites at the top and second layers. The depth of the *d*-band center of Pd site has the sequence of [Pd-metal] < [Pd_3Pb bulk] < [Pd_3Pb (110)]. This can explain the absorption of the reactant, and products will not be strongly bonded by the surface, showing a smaller ΔG (free energy profile).

However, this cannot fully explain the high ORR activity of Pd_3Pb TPs observed. This arises because the Pd-4*d* orbital is nearly inert given as $4d^{10}$. Therefore, the sole $4d^{10}$ orbital cannot play as the predominant active center for ORR catalysis, especially for the steps of electron transfer between surface and absorbing molecules. **Figure S26** shows the *sp* hybridized orbitals overlap with Pd-4*d* orbitals within the Pd_3Pb bulk system, giving more evident on the Pd_3Pb (110) surface.

Herein, it is the coupled *s-p-d* exchange effect that determines the electron transfer between the surface and absorbing molecules. The rigorous theoretical discussions of inter-orbital couplings have been widely accepted, and acted as a cornerstone for our proposed coupled *s-p-d* exchange effect.[34-37] The Goodenough-Kanamori-Anderson (GKA) orbital theory[34-37] has been firmly adapted here, and confirmed with our ab-initio orbital energy calculations through self-consistent Hubbard-type orbital projections. As from the GKA theory, the prerequisite of the inter-orbital super-exchange process is the bonding angle should be close to 90°, and must guarantee the *d*-orbital participant. In this tripod system, the Pd-Pb bonding angle within the bulk or on the surface is closely located within the range of 90°. We found this effect is even much more sensitive to the variations of Pb(*sp*)-Pd(4*d*)-Pb(*sp*) aligned bonding angle on different surfaces. Therefore, the enhanced ORR on the Pd_3Pb-(110) surface predominantly originates from the enhanced *s-p-d* exchange coupling. This orbital exchange effect leads to the stronger activity of $4d^{10}$ electrons of Pd to be transferred between the reacting surface and absorbing molecules, irregardless of its inertness from conventional viewpoint. The super-exchange model has been widely used for interpreting the anti-ferromagnetism effect of the 3*d*- or even 4*f*-orbital based metal oxides.[31-33]

In order to interpret electronic transfer mechanism of the TP surface, the electronic occupancy on the targeted orbital described in GKA theory can be translated into the electronegativity of such orbital through the theory of Parr-Donnelly-Levy-Palke (PDLP).[38] This super-exchange coupling effect can be valid within any given orbitals beyond the conventional view on the inert closed-shell of Pd-$4d^{10}$. With

illustration on orbital energy by our ab-initio calculation, any sensitive change of electronegativity on the Pd-4*d* from different bonding environment can be demonstrated, though the closed-shell effect of Pd-4d^{10} remains. Thus, the variation in orbital energy is quantitatively presented by the abnormal electronegativity fluctuation through such coupled *s*-*p*-*d* exchange effect.

This potentially denotes a fast-redox process for the electron transfer. With the electron transferred from the hybridized *sp*-orbital onto the absorbed molecule, the Pd-4d^{10} orbital turns to be active and promotes the *d*-electrons to the *sp*-orbital for further step of charge transfer *via* our proposed coupled *s*-*p*-*d* exchange effect.

(4) Pd-4*d* orbital energy as an indicator of the coupled *s*-*p*-*d* exchange effect

We previously devised a method to ab-initially determine the semicore *d*/*f* orbital energy in order to further self-consistently correct the electronic structures from routine first-principles calculations.[29, 30] Our work shows that the method is particularly valid for those materials synthesized *via* the extremely physical or chemical conditions.[29, 30] Herein, we utilized this method to ultimately reflect the total energy of the specifically targeted orbital especially with electronic occupation under a variety case of chemical bonding. With chosen ab-initio generated norm-conserving pseudopotentials by OPIUM code, we projected out the two Hubbard potential components on the orbitals by linear response method. One is the orbital chemical potential, and another is the pseudo-charge induced perturbed potential. This

method has been further developed to determine the onsite Coulomb type screened Hubbard potential of orbitals.[29, 30]

There has been a consideration whether the configuration of valence electrons of Pd is the $4d^{10}$ or $4d^{8}5s^{2}$. Thus, it is necessary to elucidate the hidden significant information on the different orbitals (*e.g.* Pd-4*d*) under the different bonding system. It not only illustrates the Pd-4*d* orbital onsite screens Coulomb potential for the targeted Pb site in bulk-Pd_3Pb, Pd, and surface-Pd_3Pb, but also facilitates our understanding on the variation of orbital energy. **Figure S27** shows the crossover point for the Hubbard potential projection of the Pd-4*d* orbital, denoting a close-shell effect for the 4*d* orbital of Pd site in Pd_3Pb *fcc* lattice. Therefore, the configuration of Pd-4*d* orbital is confirmed to be $4d^{10}$ within Pd_3Pb structure, and the Hubbard potential (Hubbard-U) parameter is self-consistently determined to be 7.54 eV for Pd-4*d* orbital.

From the calculation in **Figure S27**, the self-consistently obtained orbital energy of Pd-4*d* is found to be increased from previous 7.54 eV in the bulk to 10.12 eV on the (110) surface. However, the Pd-4*d* orbital energy on the Pd_3Pb (100) surface is found to be 6.32 eV, showing a relatively weaker Coulomb potential given by the closed-shell electronic negativity. This energetic contrast between different surfaces as well as a comparison between surface and bulk indicates the electrons on the Pd-4*d* orbital turns to be more localized on (110) surface due to the orbital overlapping *via s-p-d* exchange, which transfers the electrons *via* inter-orbitals even more evidently between Pd-Pb sites.

Characterization

Power X-ray diffraction (PXRD) patterns were collected using an X`Pert-Pro X-ray powder diffractometer equipped with a Cu radiation source (λ = 0.15406 nm). The morphology and size of the nanocrystals were determined by transmission electron microscope (TEM, Hitachi, HT7700) at 120 kV. High-resolution TEM (HRTEM), selected-area electron diffraction (SAED), TEM energy dispersive X-ray spectroscopy (TEM-EDS) and high angle annular dark field scanning TEM (HAADF-STEM) were conducted on a FEI Tecnai F20 transmission electron microscope at an acceleration voltage of 200 kV. The TEM work in Brookhaven are performed with a JEOL-2100F (for HRTEM and SAED), a FEI Talos (3D STEM tomography) and aberration corrected HD-2700C (high resolution STEM imaging and STEM-EELS mapping) at an acceleration voltage of 200 kV. All the samples were prepared by dropping cyclohexane dispersion of samples onto carbon-coated copper grids and dried under ambient condition. Low-resolution energy dispersive X-ray spectroscopy was performed on a scanning electron microscope (SEM, Hitachi, S-4700). The concentration of each catalyst was determined by the inductively coupled plasma atomic emission spectroscopy (710-ES, Varian, ICP-AES).

SUPPLEMENTAL INFORMATION

Supplemental Information includes 28 figures and 3 tables and can be found with this article online.

AUTHOR CONTRIBUTIONS

X.H and S. G. conceived and supervised the research. X.H. and L.B. designed the experiments. X.H., S. G., L.B. and Q.S. performed most of the experiments and data analysis. D.S., H.X. and S.H. performed electron microscopy analysis. X.H., S. G., L.B., Q.S., Y.P., J.Y. and J. L. participated in various aspects of the experiments and discussions. B.H. performed the DFT simulations. X.H., S. G., L.B. and Q.S. wrote the paper. All authors discussed the results and commented on the manuscript.

ACKNOWLEDGMENTS

This work was financially supported by the Ministry of Science and Technology (2016YFA0204100, 2017YFA0208200), the National Natural Science Foundation of China (21571135 and 51671003), the National Key Research and Development Program of China (No. 2016YFB0100201), Young Thousand Talented Program, the start-up supports from Soochow University, and the Priority Academic Program Development of Jiangsu Higher Education Institutions (PAPD). Part of the electron microscopy work was performed at the Center for Functional Nanomaterials, Brookhaven National Laboratory, which is supported by the U.S. Department of Energy (DOE), Office of Basic Energy Science, under contract DE-SC0012704.

REFERENCES AND NOTES

[1] Winter, M. and Brodd, R. J. (2004). What are batteries, fuel cells, and supercapacitors? Chem. Rev. *104*, 4245-4270.

[2] Arico, A. S., Bruce, P., Scrosati, B., Tarascon, J. M. and Van Schalkwijk, W. (2005). Nanostructured materials for advanced energy conversion and storage devices. Nat. Mater. *4*, 366-377.

[3] Mai, L. Q., Tian, X. C., Xu, X., Chang, L. and Xu, L. (2014). Nanowire electrodes for electrochemical energy storage devices. Chem. Rev. *114*, 11828-11862.

[4] Chen, D. J., Chen, C., Baiyee, Z. M., Shao, Z. P. and Ciucci, F. (2015). Nonstoichiometric oxides as low-cost and highly-efficient oxygen reduction/evolution catalysts for low-temperature electrochemical devices. Chem. Rev. *115*, 9869-9921.

[5] Cheng, F. Y., Shen, J., Peng, B., Pan, Y. D., Tao, Z. L. and Chen, J. (2011). Rapid room-temperature synthesis of nanocrystalline spinels as oxygen reduction and evolution electrocatalysts. Chen, Nat. Chem. *3*, 79-84.

[6] Liang, Y. Y., Li, Y. G., Wang, H. L., Zhou, J. G., Wang, J., Regier, T. and Dai, H. J. (2011). Co_3O_4 nanocrystals on graphene as a synergistic catalyst for oxygen reduction reaction. Nat. Mater. *10*, 780-786.

[7] Bruce, P. G., Freunberger, S. A., Hardwick, L. J. and Tarascon, J. -M. (2012). Li-O_2 and Li-S batteries with high energy storage. Nat. Mater. *11*, 19-29.

[8] Duan, J. J., Chen, S., Jaroniec, M. and Qiao, S. Z. (2015). Heteroatom-doped graphene-based materials for energy-relevant electrocatalytic processes. ACS Catal. *5*, 5207-5234.

[9] Stamenkovic, V. R., Mun, B. S., Arenz, M., Mayrhofer, K. Z. Z., Lucas, C. A., Wang, G. F., Ross, P. N. and Marković, N. M. (2007). Trends in electrocatalysis on extended and nanoscale Pt-bimetallic alloy surfaces. Nat. Mater. *6*, 241-247.

[10] Stamenkovic, V. R., Fowler, B., Mun, B. S., Wang, G. F., Ross, P. N., Lucas, C. A. and Marković, N. M. (2007). Improved oxygen reduction activity on $Pt_3Ni(111)$ via increased surface site availability. Science *315*, 493-497.

[11] Greeley, J., Stephens, I. E. L., Bondarenko, A. S., Johansson, T. P., Hansen, H. A., Jaramillo, T. F., Rossmeisl, J., Chorkendorff, I. and Nørskov, J. K. (2009). Alloys of platinum and early transition metals as oxygen reduction electrocatalysts. Nat. Chem. *1*, 552-556.

[12] Ge, X. M., Sumboja, A., Wuu, D., An, T., Li, B., Thomas Goh, F. W., Andy Hor, T. S., Zong, Y. and Liu, Z. L. (2015). Oxygen reduction in alkaline media: from mechanisms to recent advances of catalysts. ACS Catal. *5*, 4643-4667.

[13] Wang, Y. J., Zhao, N. N., Fang, B. Z., Li, H., Bi, X. T. T. and Wang, H. J. (2015). Carbon-supported Pt-based alloy electrocatalysts for the oxygen reduction reaction in polymer electrolyte membrane fuel cells: particle size, shape, and composition manipulation and their impact to activity. Chem. Rev. *115*, 3433-3467.

[14] Shao, M. H., Chang, Q. W., Dodelet, J. -P. and Chenitz, R. (2016). Recent advances in electrocatalysts for oxygen reduction reaction. Chem. Rev. *116*, 3594-3657.

[15] Wu, G., More, K. L., Johnston, C. M. and Zelenay, P. (2011). High-performance electrocatalysts for oxygen reduction derived from polyaniline, iron, and cobalt. Science *332*, 443-447.

[16] Li, Y. G., Zhou, W., Wang, H. L., Xie, L. M., Liang, Y. Y., Wei, F., Idrobo, J. -C., Pennycook, S. J. and Dai, H. J. (2012). An oxygen reduction electrocatalyst based on carbon nanotube-graphene complexes. Nat. Nanotechnol. *7*, 394-400.

[17] Wu, Z. S., Yang, S. B., Sun, Y., Parvez, K., Feng, X. L. and Müllen, K. (2012). 3D nitrogen-doped graphene aerogel-supported Fe_3O_4 nanoparticles as efficient electrocatalysts for the oxygen reduction reaction. J. Am. Chem. Soc. *134*, 9082-9085.

[18] Li, Q., Cao, R. G., Cho, J. and Wu, G. (2014). Nanocarbon electrocatalysts for oxygen reduction in alkaline media for advanced energy conversion and storage. Adv. Energy Mater. *4*, 1301415.

[19] Jiang, G. M., Zhu, H. Y., Zhang, X., Shen, B., Wu, L. H., Zhang, S., Lu, G., Wu, Z. B. and Sun, S. H. (2015). Core/shell face-centered tetragonal FePd/Pd nanoparticles as an efficient non-Pt catalyst for the oxygen reduction reaction. ACS Nano *9*, 11014-11022.

[20] Poon, K. C., Tan, D. C. L., Vo, T. D. T., Khezri, B., Su, H. B., Webster, R. D. and Sato, H. (2014). Newly developed stepwise electroless deposition enables a remarkably facile synthesis of highly active and stable amorphous Pd nanoparticle electrocatalysts for oxygen reduction reaction. J. Am. Chem. Soc. *136*, 5217-5220.

[21] Lu, Y. Z., Jiang, Y. Y., Gao, X. H., Wang, X. D. and Chen, W. (2014). Strongly coupled Pd nanotetrahedron/tungsten oxide nanosheet hybrids with enhanced catalytic activity and stability as oxygen reduction electrocatalysts. J. Am. Chem. Soc. *136*, 11687-11697.

[22] Furukawa, S., Suga, A. and Komatsu, T. (2015). Mechanistic study on aerobic oxidation of amine over intermetallic Pd_3Pb: concerted promotion effects by Pb and support basicity. ACS Catal. *5*, 1214-1222.

[23] Antolini, E. (2009). Palladium in fuel cell catalysis. Energy Environ. Sci. *2*, 915-931.

[24] Cui, Z. M., Chen, H., Zhao, M. T. and DiSalvo, F. J. (2016). High-performance Pd_3Pb intermetallic catalyst for electrochemical oxygen reduction. Nano Lett. *16*, 2560-2566.

[25] Nørskov, J. K., Rossmeisl, J., Logadottir, A., Lindqvist, L., Kitchin, J. R., Bligaard, T. and Jónsson, H. (2004). Origin of the overpotential for oxygen reduction at a fuel-cell cathode. J. Phys. Chem. B *108*, 17886-17892.

[26] Sidik, R. A. and Anderson, A. B. (2002). Density functional theory study of O_2 electroreduction when bonded to a Pt dual site. J. Electroanal. Chem. *528*, 69-76.

[27] Lamas, E. J. and Balbuena, P. B. (2006). Oxygen reduction on $Pd_{0.75}Co_{0.25}$ (111) and $Pt_{0.75}Co_{0.25}$ (111) surfaces: an ab initio comparative study. J. Chem. Theory Comput. *2*, 1388-1394.

[28] Stamenkovic, V., Mun, B. S., Mayrhofer, K. J. J., Ross, P. N., Markovic, N. M., Rossmeisl, J., Greeley, J. and Nørskov, J. K. (2006). Changing the activity of electrocatalysts for oxygen reduction by tuning the surface electronic structure. Angew. Chem. Int. Ed. *45*, 2897-2901.

[29] Huang, B. (2016). 4f fine-structure levels as the dominant error in the electronic structures of binary lanthanide oxides. J. Comput. Chem. *37*, 825-835.

[30] Huang, B. (2017). The screened pseudo-charge repulsive potential in perturbed orbitals for band calculations by DFT+U. Phys. Chem. Chem. Phys. *19*, 8008-8025.

[31] Du, X. S., Li, Q. X., Su, H. B. and Yang, J. L. (2006). Electronic and magnetic properties of V-doped anatase TiO_2 from first principles. Phys. Rev. B *74*, 233201.

[32] Han, X. P., Lee, J. C. and Yoo, H. -I. (2009). Oxygen-vacancy-induced ferromagnetism in CeO_2 from first principles. Phys. Rev. B *79*, 100403.

[33] Janisch, R. and Spaldin, N. A. (2006). Understanding ferromagnetism in Co-doped TiO_2 anatase from first principles. Phys. Rev. B *73*, 035201.

[34] Goodenough, J. B. (1963). *Magnetism and the Chemical Bond* (Inter-science, New York).

[35] Anderson, P. W. (1950). Antiferromagnetism. Theory of superexchange interaction. Phys. Rev. *79*, 350-356.

[36] Goodenough, J. B. (1955). Theory of the role of covalence in the perovskite-type manganites [La, *M*(II)]MnO_3. Phys. Rev. *100*, 564-573.

[37] Kanamori, J. (1959). Superexchange interaction and symmetry properties of electron orbitals. J. Phys. Chem. Solids *10*, 87-98.

[38] Parr, R. G., Donnelly, R. A., Levy, M. and Palke, W. E. (1978). Electronegativity: the density functional viewpoint. J. Chem. Phys. *68*, 3801-3807.